Towards pure near-infrared to near-infrared upconversion of multifunctional GdF$_3$:Yb^{3+},Tm^{3+} nanoparticles

Hon-Tung Wong, Helen Lai Wa Chan, and Jianhua Hao*

Department of Applied Physics and Materials Research Centre, The Hong Kong Polytechnic University, Hong Kong, People's Republic of China
*apjhhao@polyu.edu.hk

Abstract: Nearly pure near-infrared to near-infrared (NIR-to-NIR) upconversion in GdF$_3$ host with 23% Yb^{3+} and 1% Tm^{3+} under 980 nm excitation is firstly reported. The ratio of the intensity of the emission at 807 nm to that at 478 nm can reach to 105, and the intensity of the emission at 807 nm is preserved. Moreover, the excitation and the emission at 980 and 807 nm are away from the visible region. These are beneficial to deeper tissue penetration and reduced autofluorescence. Raman spectroscopy measurements suggest the high probability of NIR emission in GdF$_3$ host. Our results indicate that the reported multifunctional nanoparticles are promising in bio-imaging and bio-separation.

©2010 Optical Society of America

OCIS codes: (160.5690) Rare-earth-doped materials; (190.4180) Multiphoton processes; (190.7220) Upconversion.

References and links

1. M. Nyk, R. Kumar, T. Y. Ohulchanskyy, E. J. Bergey, and P. N. Prasad, "High contrast in vitro and in vivo photoluminescence bioimaging using near infrared to near infrared up-conversion in Tm^{3+} and Yb^{3+} doped fluoride nanophosphors," Nano Lett. **8**(11), 3834–3838 (2008).
2. R. Weissleder, "A clearer vision for in vivo imaging," Nat. Biotechnol. **19**(4), 316–317 (2001).
3. C. T. Xu, N. Svensson, J. Axelsson, P. Svenmarker, G. Somesfalean, G. Y. Chen, H. J. Liang, H. C. Liu, Z. G. Zhang, and S. Andersson-Engels, "Autofluorescence insensitive imaging using upconverting nanocrystals in scattering media," Appl. Phys. Lett. **93**(17), 171103 (2008).
4. S. Heer, K. Kompe, H. U. Gudel, and M. Haase, "Highly efficient multicolour upconversion emission in transparent colloids of lanthanide-doped NaYF$_4$ nanocrystals," Adv. Mater. **16**(23–24), 2102–2105 (2004).
5. Z. Q. Li, and Y. Zhang, "Monodisperse silica-coated polyvinylpyrrolidone/NaYF$_4$ nanocrystals with multicolor upconversion fluorescence emission," Angew. Chem. Int. Ed. **45**(46), 7732–7735 (2006).
6. F. Wang, and X. G. Liu, "Recent advances in the chemistry of lanthanide-doped upconversion nanocrystals," Chem. Soc. Rev. **38**(4), 976–989 (2009).
7. P. N. Prasad, *Introduction to biophotonics* (Wiley-Interscience, 2003).
8. X. K. Shu, A. Royant, M. Z. Lin, T. A. Aguilera, V. Lev-Ram, P. A. Steinbach, and R. Y. Tsien, "Mammalian expression of infrared fluorescent proteins engineered from a bacterial phytochrome," Science **324**(5928), 804–807 (2009).
9. B. W. Rice, and C. H. Contag, "The importance of being red," Nat. Biotechnol. **27**(7), 624–625 (2009).
10. K. W. Kramer, D. Biner, G. Frei, H. U. Gudel, M. P. Hehlen, and S. R. Luthi, "Hexagonal sodium yttrium fluoride based green and blue emitting upconversion phosphors," Chem. Mater. **16**(7), 1244–1251 (2004).
11. H. T. Wong, H. L. W. Chan, and J. H. Hao, "Magnetic and luminescent properties of multifunctional GdF$_3$:Eu^{3+} nanoparticles," Appl. Phys. Lett. **95**(2), 022512 (2009).
12. D. Dosev, M. Nichkova, R. K. Dumas, S. J. Gee, B. D. Hammock, K. Liu, and I. M. Kennedy, "Magnetic/luminescent core/shell particles synthesized by spray pyrolysis and their application in immunoassays with internal standard," Nanotechnology **18**(5), 055102 (2007).
13. Z. Y. Liu, G. S. Yi, H. T. Zhang, J. Ding, Y. W. Zhang, and J. M. Xue, "Monodisperse silica nanoparticles encapsulating upconversion fluorescent and superparamagnetic nanocrystals," Chem. Commun. (Camb.) **6**(6), 694–696 (2008).
14. C. T. Xu, J. Axelsson, and S. Andersson-Engels, "Fluorescence diffuse optical tomography using upconverting nanoparticles," Appl. Phys. Lett. **94**(25), 251107 (2009).
15. F. Wang, and X. G. Liu, "Upconversion multicolor fine-tuning: visible to near-infrared emission from lanthanide-doped NaYF$_4$ nanoparticles," J. Am. Chem. Soc. **130**(17), 5642–5643 (2008).
16. R. Kumar, M. Nyk, T. Y. Ohulchanskyy, C. A. Flask, and P. N. Prasad, "Combined optical and MR bioimaging using rare earth ion doped NaYF$_4$ nanocrystals," Adv. Funct. Mater. **19**(6), 853–859 (2009).

17. T. Miyakawa, and D. L. Dexter, "Cooperative and stepwise excitation of luminescence: Trivalent rare-earth ions in Yb^{3+}-sensitized crystals," Phys. Rev. B **1**(1), 70–80 (1970).
18. W. S. Tsang, W. M. Yu, C. L. Mak, W. L. Tsui, K. H. Wong, and H. K. Hui, "Evidence of the influence of phonon density on Tm^{3+} upconversion luminescence in tellurite and germanate glasses," J. Appl. Phys. **91**(4), 1871–1874 (2002).
19. W. M. Yen, and P. M. Selzer, *Laser spectroscopy of solids, topics in applied physics* (Springer-Verlag, 1986).
20. G. F. Wang, W. P. Qin, J. S. Zhang, J. S. Zhang, Y. Wang, C. Y. Cao, L. L. Wang, G. D. Wei, P. F. Zhu, and R. J. Kim, "Synthesis, growth mechanism, and tunable upconversion luminescence of Yb^{3+}/Tm^{3+}-codoped YF_3 nanobundles," J. Phys. Chem. C **112**(32), 12161–12167 (2008).
21. D. Q. Chen, Y. S. Wang, Y. L. Yu, and P. Huang, "Intense ultraviolet upconversion luminescence from Tm^{3+}/Yb^{3+}:β-YF_3 nanocrystals embedded glass ceramic," Appl. Phys. Lett. **91**(5), 051920 (2007).
22. C. X. Li, J. Yang, P. P. Yang, H. Z. Lian, and J. Lin, "Hydrothermal synthesis of lanthanide fluorides LnF_3 (Ln = La to Lu) nano-/microcrystals with multiform structures and morphologies," Chem. Mater. **20**(13), 4317–4326 (2008).
23. C. X. Li, Z. W. Quan, P. P. Yang, J. Yang, H. Z. Lian, and J. Lin, "Shape controllable synthesis and upconversion properties of $NaYbF_4/NaYbF_4$: Er^{3+} and YbF_3/YbF_3: Er^{3+} microstructures," J. Mater. Chem. **18**(12), 1353–1361 (2008).

1. Introduction

The light absorption coefficient of biological tissues (e.g. hemoglobin) is minimum in near-infrared (NIR) region (750 – 1000 nm) [1–7]. It is reported that NIR radiation can travel at least 10 cm through breast tissue, and 4 cm of skull/brain tissue or deep muscle using microwatt laser sources. These penetration depths cannot be achieved with the use of ultraviolet (UV) and visible light [2,6]. It is therefore desirable to produce nanoparticles with both excitation and emission of luminescences in the NIR region for in vitro and in vivo imaging applications. This will consequently lead to deeper light penetration, reduced autofluorescence from the biological tissues, reduced light scattering, and thus, increased image contrast [1–7]. In a recent study reported by Tsien's group, utilization of NIR fluorescent proteins for pure NIR excitation and emission was achieved [8]. The views that the achieved NIR excitation and emission are still too close to the visible region were pointed out by Tsien. It has been indicated that further increase of both the NIR excitation and emission to longer wavelengths will be a trend in NIR bio-imaging, which is advantageous for deeper penetration through thicker and more complex tissues [2,6,8,9].

Upconversion is uniquely exhibited by rare-earth (RE) doped nanoparticles [1,6]. However, the nearly or fully pure NIR-to-NIR upconversion (NIR excitation; NIR emission) was still unattainable in RE-doped nanoparticles. There was little study on the mechanisms elucidating the prominent NIR-to-visible ratio, which is defined as the ratio of the intensity of the NIR emission to that of the visible emission. A recent study utilizing $NaYF_4$:Yb^{3+},Tm^{3+} nanoparticles as an efficient host for upconversion only exhibited a NIR-to-visible ratio of about 3 [1,10]. The accompanying simultaneous visible emission at around 478 nm is well located inside the absorption region of flavins, which are endogenous fluorophores native to cells for autofluorescence with a maximum emission at around 550 nm [7]. The relatively strong visible emission at 478 nm would cause autofluorescence of the flavins. It is therefore desirable to increase the NIR-to-visible ratio by suppressing the intensity of the visible emission. Furthermore, nearly pure NIR-to-NIR upconverting multifunctional nanoparticles with both luminescent and magnetic properties are seldom reported [11–13]. Besides, autofluorescence causes severe problems in, especially the ill-posed, fluorescence diffuse optical tomography (FDOT). Moreover, FDOT utilizing upconverting $NaYF_4$:Yb^{3+},Tm^{3+} nanoparticles for reduction of autofluorescence was recently reported [14]. In this work, multifunctional GdF_3:Yb^{3+},Tm^{3+} nanoparticles showing both nearly pure NIR-to-NIR upconversion (with a high NIR-to-visible ratio I_{807nm}/I_{478nm} of about 105 and preserved I_{807nm}) and magnetic property are reported. Possible physical mechanism elucidating the prominent NIR-to-visible ratio is discussed. Magnetization as a function of an applied magnetic field is also determined.

2. Results and discussion

The GdF_3: x Yb^{3+}, y Tm^{3+} nanoparticles ($x = 20$, 23 mol%; $y = 0.5$, 1, 2, 3 mol%) were prepared using hydrothermal synthesis. An X-ray diffraction (XRD) pattern of the GdF_3:23%Yb^{3+},1%Tm^{3+} nanoparticles is shown in Fig. 1(a). The diffraction pattern is in good agreement with a JCPDS standard card (no. 12-0788) of an orthorhombic GdF_3 crystal phase and space group *Pnma*. The obtained nanoparticles are mainly composed of elongated nanoparticles, with a small proportion of spherical and nearly spherical nanoparticles. The average length and width of the elongated nanoparticles are around 100 and 50 nm, respectively; while the average sizes of the spherical and nearly spherical nanoparticles are around 40 nm (Fig. 1(b)). The homogeneous distribution of the Yb^{3+} and Tm^{3+} dopant ions in the GdF_3:Yb^{3+},Tm^{3+} nanoparticles is supported by the SEM element mapping images (not shown). It is because there is no preferred location of Yb^{3+} and Tm^{3+} dopant ions in GdF_3 host during crystal growth. Also, the colloidal solution of $Gd(NO_3)_3$, $Yb(NO_3)_3$, $Tm(NO_3)_3$ solutions and NaF particles were vigorously stirred for 2 h before hydrothermal treatment.
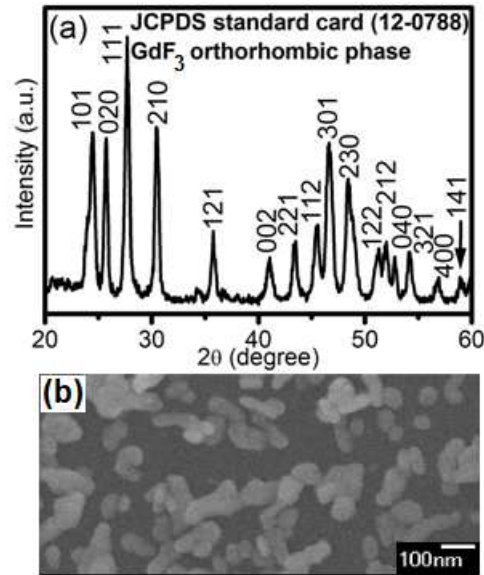

Fig. 1. (a) XRD pattern of the GdF_3:23%Yb^{3+},1%Tm^{3+} nanoparticles with the dominant peaks labeled. (b) FE-SEM image of the GdF_3:23%Yb^{3+},1%Tm^{3+} nanoparticles.
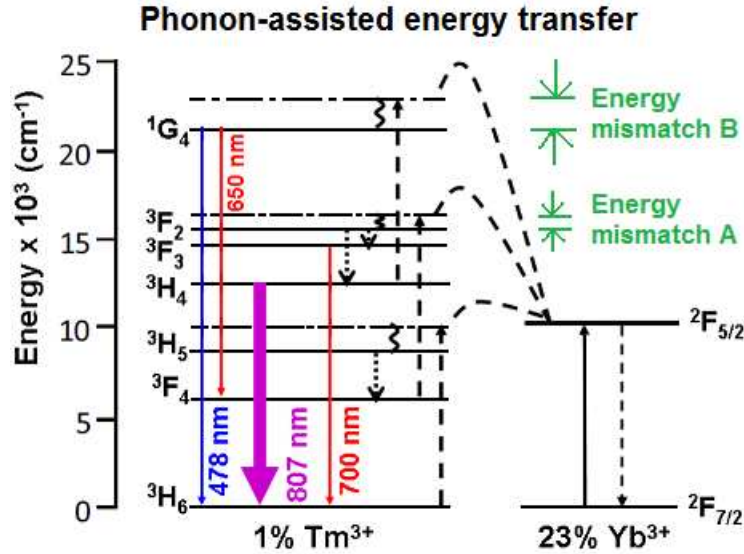
Fig. 2. (Color online) The upconversion mechanisms of the dopants of the Yb^{3+} and Tm^{3+} ions under 980 nm CW laser excitation (90 mW). $GdF_3:23\%Yb^{3+},1\%Tm^{3+}$ with dominant emission at 807 nm is shown as an example. The upward solid, downward solid, dashed, dotted, and curly solid arrows represent excitation, emission, phonon assisted energy transfer, multiphonon relaxation, and energy mismatch between the transitions within the Yb^{3+} and the Tm^{3+} ions, respectively.
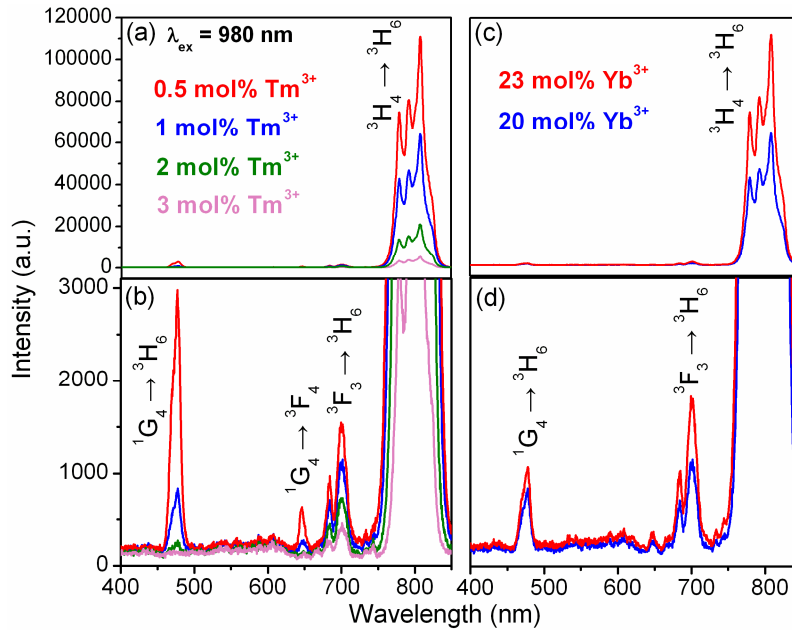
Fig. 3. (Color online) (a) Room temperature photoluminescent emission spectra of the GdF_3: 20% Yb^{3+}, y Tm^{3+} (y = 0.5, 1, 2, 3 mol%) nanoparticles excited at 980 nm (90 mW). (b) The corresponding magnified part illustrating the weak visible light emission in (a). (c) Room temperature photoluminescent emission spectra of the GdF_3: x Yb^{3+}, 1% Tm^{3+} (x = 20, 23 mol%) nanoparticles excited at 980 nm (90 mW). (d) The corresponding magnified part illustrating the weak visible light emission in (c). The vertical scale of (c) is the same as that of (a), and the vertical scale of (d) is the same as that of (b).

Table 1. Optimization of the NIR-to-visible ratios through variations in dopants concentrations: (a) Variation in Tm^{3+} doping concentration in GdF$_3$: 20% Yb^{3+}, y Tm^{3+} (y = 0.5, 1, 2, 3 mol%), and (b) variation in Yb^{3+} doping concentration in GdF$_3$: x Yb^{3+}, 1% Tm^{3+} (x = 20, 23 mol%).

(a) Variation in Tm^{3+} doping concentration in GdF$_3$: 20% Yb^{3+}, y Tm^{3+}.

NIR-to-visible ratios	Tm^{3+} doping concentration (mol%)			
	0.5	1	2	3
I$_{807\,nm}$ / I$_{478\,nm}$	37	76	77	N/A
I$_{807\,nm}$ / I$_{650\,nm}$	176	N/A	N/A	N/A
I$_{807\,nm}$ / I$_{700\,nm}$	72	56	29	12

(b) Variation in Yb^{3+} doping concentration in GdF$_3$: x Yb^{3+}, 1% Tm^{3+}.

NIR-to-visible ratios	Yb^{3+} doping concentration (mol%)	
	20	23
I$_{807\,nm}$ / I$_{478\,nm}$	76	105
I$_{807\,nm}$ / I$_{650\,nm}$	N/A	N/A
I$_{807\,nm}$ / I$_{700\,nm}$	56	61

Photoluminescent emission (PL; excited with a NIR 980 nm CW laser diode of 90 mW) spectra of the GdF$_3$: x Yb^{3+}, y Tm^{3+} nanoparticles were measured by an Edinburgh Instruments FLSP920 spectrofluorometer. The energy transfer mechanisms responsible for the upconversion emissions in GdF$_3$:Yb^{3+},Tm^{3+} are shown in Fig. 2. A series of characteristic emission peaks of the Tm^{3+} ions ranging from visible blue to NIR are clearly observed in Fig. 3, with the dominant emission at 807 nm. The NIR-to-visible ratio is increased through the optimization of the dopant concentrations (Table 1), which is a common method of fine tuning the NIR-to-visible ratio [6,15,16]. It is clearly seen that the absolute intensity of the NIR emission I$_{807nm}$ of GdF$_3$:23%Yb^{3+},1%Tm^{3+} is almost the same as that of GdF$_3$:20%Yb^{3+},0.5%Tm^{3+} and remains the highest among different dopant concentrations (Fig. 3). It is also noted that I$_{478nm}$ decreases significantly and the NIR-to-visible ratio (I$_{807nm}$/I$_{478nm}$) ultimately reaches a remarkable value of 105 in GdF$_3$:23%Yb^{3+},1%Tm^{3+}. This may be due to the enhanced population of the $^3H_4$ state and increased energy transfer efficiency from the Yb^{3+} to the Tm^{3+} ions [15]. The enhanced population of the $^3H_4$ state is caused by energy resonance between the $^1G_4 \rightarrow {}^3H_4$ and $^3F_2 \leftarrow {}^3F_4$ (Fig. 2) with the increase of the Tm^{3+} doping concentration from 0.5 to 1 mol% in the GdF$_3$: 20% Yb^{3+}, y Tm^{3+} nanoparticles (y = 0.5, 1, 2, 3 mol%) [15]. This enhanced population of the $^3H_4$ state primarily enhances the intensity of the NIR emission (I$_{807nm}$; $^3H_4 \rightarrow {}^3H_6$), and at the same time, it leads to the decreases in the intensities of the visible emissions of I$_{478nm}$ ($^1G_4 \rightarrow {}^3H_6$) and I$_{650nm}$ ($^1G_4 \rightarrow {}^3F_4$). Further increase in the Tm^{3+} doping concentration leads to the dominance of concentration quenching, which turns out to suppress the NIR-to-visible ratio (I$_{807nm}$/I$_{478nm}$). Another NIR-to-visible ratio (I$_{807nm}$/I$_{700nm}$) continuously decreases with the increase in the Tm^{3+} doping concentration due to the influence of the concentration quenching only. The increased energy transfer efficiency from the Yb^{3+} to the Tm^{3+} ions is achieved with the increase of the Yb^{3+} doping concentration to 23 mol% in the GdF$_3$: x Yb^{3+}, 1% Tm^{3+} nanoparticles (x = 20, 23 mol%). This amplifies the effect of the enhanced population of the $^3H_4$ state, and thus, the NIR-to-visible ratio (I$_{807nm}$/I$_{478nm}$) reaches to 105 in GdF$_3$:23%Yb^{3+},1%Tm^{3+}. The remarkable NIR-to-visible ratio of 105 has not yet been reported in other hosts, including the highly efficient and intensively studied NaYF$_4$ [3,15].

In addition to the effect of the dopant concentration, it is believed that the effects of the intrinsically larger probability of the phonon assisted energy transfer leading to the NIR emission [17] and the phonons of the GdF$_3$ host [18,19] contribute to the remarkable NIR-to-visible ratio of 105 obtained in the GdF$_3$:23%Yb^{3+},1%Tm^{3+} (Figs. 2 and 4(a)). The probability of the phonon assisted energy transfer from the Yb^{3+} ions to the Tm^{3+} ions decreases exponentially with the increase in the energy mismatch between the transitions within the Yb^{3+} ($^2F_{7/2} \rightarrow {}^2F_{5/2}$) and the Tm^{3+} ($^3H_6 \rightarrow {}^3H_5$, $^3F_4 \rightarrow {}^3F_2$ and $^3H_4 \rightarrow {}^1G_4$). As the energy mismatch for the $^3F_4 \rightarrow {}^3F_2$ (1000 cm^{-1}; denoted as energy mismatch A in Fig. 2) is smaller than that for the $^3H_4 \rightarrow {}^1G_4$ (1800 cm^{-1}; denoted as energy mismatch B in Fig. 2), the probability of the phonon assisted energy transfer leading to the NIR emission is intrinsically

larger (Fig. 2) [17]. Furthermore, the probability of the phonon assisted energy transfer from Yb^{3+} to Tm^{3+} decreases with the number of phonons of the hosts required to fill up the energy mismatch [17–19], which may be the factor that determines different NIR-to-visible ratios for different hosts of the same dopants and dopant concentrations. The number of phonons required is an intrinsic property of the host which can be estimated from the Raman spectrum of the host.

To verify the above mechanism, a comparison on the Raman spectra between GdF_3 and YF_3 hosts (Fig. 4(a)) is carried out since both hosts co-doped with Yb^{3+}/Tm^{3+} are in the same crystal phase, i.e. orthorhombic (not shown), and $YF_3:Yb^{3+},Tm^{3+}$ nanoparticles are reported to exhibit intense NIR-to-UV upconversion (NIR excitation; UV emission) [20,21]. Here, GdF_3, YF_3 and $YF_3:23\%Yb^{3+},1\%Tm^{3+}$ were all prepared using hydrothermal synthesis. The influence of the phonons of the hosts on the NIR-to-visible ratios is demonstrated. The phonon modes with energies around 333.3 and 360 cm^{-1} of the GdF_3 host and 250 and 450 cm^{-1} of the YF_3 host are responsible for the NIR-to-visible ratios (Fig. 4(a)). For the energy mismatch of the $^3H_4 \rightarrow {}^1G_4$ transition of 1800 cm^{-1} (denoted as energy mismatch B in Fig. 2) [17], four phonons with energy of 450 cm^{-1} for the YF_3 host and five phonons with energy of 360 cm^{-1} for the GdF_3 host are required to fill up the energy mismatch. As higher numbers of phonons of the GdF_3 host are required to fill up the energy mismatch, this suggests that the probability of the phonon assisted energy transfer leading to the emissions at 478 and 650 nm ($^3H_4 \rightarrow {}^1G_4$) for the $GdF_3:23\%Yb^{3+},1\%Tm^{3+}$ is smaller than that for the $YF_3:23\%Yb^{3+},1\%Tm^{3+}$. While four phonons with energy of 250 cm^{-1} for the YF_3 host and three phonons with energy of 333.3 cm^{-1} for the GdF_3 host are required to fill up the energy mismatch of the $^3F_4 \rightarrow {}^3F_2$ transition at 1000 cm^{-1} (denoted as energy mismatch A in Fig. 2) [17]. This suggests a larger probability of the phonon assisted energy transfer leading to the emissions at 700 and 807 nm ($^3F_4 \rightarrow {}^3F_2$) for the $GdF_3:23\%Yb^{3+},1\%Tm^{3+}$ than that for the $YF_3:23\%Yb^{3+},1\%Tm^{3+}$. Taking the above two probabilities into account, the NIR-to-visible ratio of the $GdF_3:23\%Yb^{3+},1\%Tm^{3+}$ should be larger than that of the $YF_3:23\%Yb^{3+},1\%Tm^{3+}$, which is consistent with our measured remarkable NIR-to-visible ratio of 105 in $GdF_3:23\%Yb^{3+},1\%Tm^{3+}$ versus 52 in $YF_3:23\%Yb^{3+},1\%Tm^{3+}$ (Fig. 4). It is noted that the intensity of the entire PL spectrum of the $YF_3:23\%Yb^{3+},1\%Tm^{3+}$ is larger than that of the $GdF_3:23\%Yb^{3+},1\%Tm^{3+}$ (Figs. 4(d) and 4(e)). This is probably due to a smaller unit cell volume of the YF_3 host, which causes an increase in the crystal field strength around the dopant ions and leads to an enhanced upconversion efficiency [6]. As the NIR-to-visible ratio (I_{807nm}/I_{478nm}) of the $GdF_3:23\%Yb^{3+},1\%Tm^{3+}$ is larger than that of the $YF_3:23\%Yb^{3+},1\%Tm^{3+}$, it suggests that the $GdF_3:23\%Yb^{3+},1\%Tm^{3+}$ should produce relatively smaller amount of autofluorescence as compared to the $YF_3:23\%Yb^{3+},1\%Tm^{3+}$.

Apart from the excellent performance of exhibiting nearly pure NIR-to-NIR upconversion, the $GdF_3:23\%Yb^{3+},1\%Tm^{3+}$ nanoparticles also exhibit paramagnetism at 293 K (applied field ranges from −20 to 20 kOe) due to noninteracting localized nature of the magnetic moment (Fig. 5) [11]. Detailed physical mechanisms elucidating the magnetic properties of the RE-doped GdF_3 nanoparticles have been given in our previous report [11]. The magnetization at 20 kOe (at 293 K) is around 2 emu/g, which is near to the reported value of the nanoparticles used for common bio-separation [11–13].
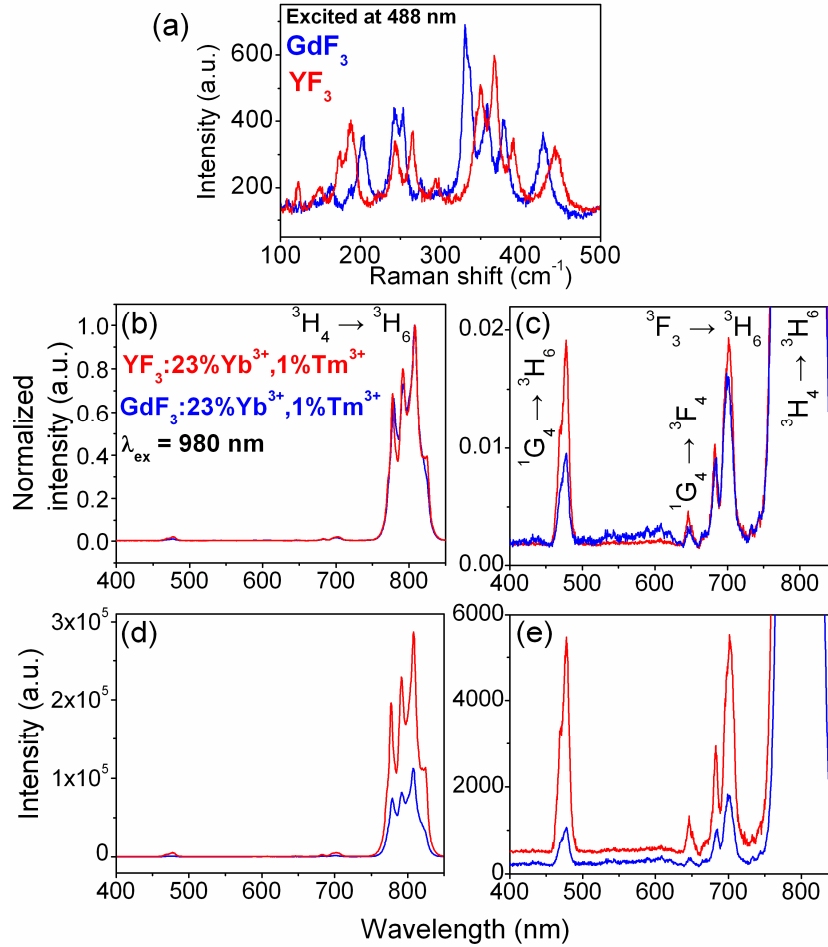
Fig. 4. (Color online) (a) Comparison on the room temperature Raman spectra between the GdF$_3$ (blue) and YF$_3$ (red) hosts excited at 488 nm. (b) Normalized room temperature photoluminescent emission spectra of the GdF$_3$:23%Yb^{3+},1%Tm^{3+} (blue) and the YF$_3$:23%Yb^{3+},1%Tm^{3+} (red) excited at 980 nm (90 mW). (c) The corresponding magnified part illustrating the weak visible light emission in (b). The NIR-to-visible ratio (I$_{807nm}$/I$_{478nm}$) of the GdF$_3$:23%Yb^{3+},1%Tm^{3+} is significantly larger than that of the YF$_3$:23%Yb^{3+},1%Tm^{3+} (105 vs. 52). (d) Room temperature photoluminescent emission spectra of the GdF$_3$:23%Yb^{3+},1%Tm^{3+} (blue) and the YF$_3$:23%Yb^{3+},1%Tm^{3+} (red) excited at 980 nm (90 mW). (e) The corresponding magnified part illustrating the weak visible light emission in (d).
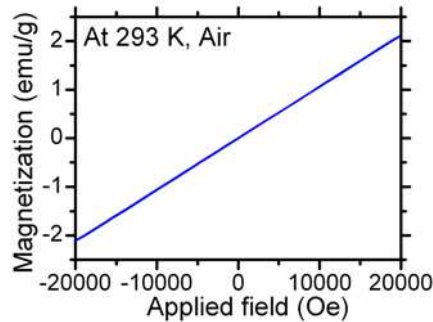

Fig. 5. Magnetization as a function of applied magnetic field of the GdF$_3$:23%Yb^{3+},1%Tm^{3+} nanoparticles at 293 K.

3. Conclusions

In conclusion, multifunctional GdF_3:Yb^{3+},Tm^{3+} nanoparticles exhibit both the nearly pure NIR-to-NIR upconversion and paramagnetism. Under 980 nm excitation, the GdF_3:23%Yb^{3+},1%Tm^{3+} nanoparticles exhibit intense NIR emission at 807 nm, while the emission at 478, 650 and 700 nm are greatly suppressed. The excellent NIR-to-visible ratio of 105 is due to the higher probability of the NIR emission, which is ascribed to the smaller number of phonons required from the GdF_3 host to fill up the energy mismatch. The NIR emission at 807 nm is away from the visible region. These are beneficial to deeper tissue penetration and reduced autofluorescence. The measured magnetization of approximately 2 emu/g is close to reported values of other nanoparticles for bio-separation. The GdF_3:Yb^{3+},Tm^{3+} nanoparticles may find potential uses in high-contrast in vitro and in vivo imaging and bio-separation.

4. Experimental methods

The syntheses of the nanoparticles were referred to some literatures with modifications [22,23]. For the synthesis of GdF_3:Yb^{3+},Tm^{3+} nanoparticles, stoichiometric amounts of $Gd(NO_3)_3$ (0.08 M, 65 mL), $Yb(NO_3)_3$, $Tm(NO_3)_3$ solutions and NaF particles were mixed in deionized (DI) water under magnetic stirring. After the NaF was dissolved, the colloidal solution was then transferred to a tightly capped beaker at 80 °C for 2 h under magnetic stirring in air. The colloidal solution was then transferred to a hydrothermal autoclave and hydrothermally treated at 180 °C under a pressure of about 700 kPa for 18 h. The obtained particle was then separated and cleaned by centrifugation (4500 rpm, 15 min) using DI water for three times, and dried at 80 °C for 12 h in air. The GdF_3, YF_3, and YF_3:Yb^{3+},Tm^{3+} were synthesized with the identical procedures with small differences in the starting materials. For the synthesis of the GdF_3 nanoparticles, only the $Gd(NO_3)_3$ and NaF were used, the procedures are the same as those of the GdF_3:Yb^{3+},Tm^{3+}. For the synthesis of the YF_3:Yb^{3+},Tm^{3+} nanoparticles, the $Y(NO_3)_3$, $Yb(NO_3)_3$, $Tm(NO_3)_3$ solutions and the NaF particles were used. While for the synthesis of the YF_3 nanoparticles, only the $Y(NO_3)_3$ and NaF were used. The procedures are identical to those of the GdF_3:Yb^{3+},Tm^{3+}.

X-ray diffraction (XRD) was carried out using a Philips Xpert System with Cu Kα radiation (λ = 1.5406 Å). Field-emission scanning electron microscope (FE-SEM) images were obtained using a JEOL-JSM 6335F. Room temperature photoluminescent spectra were taken with an Edinburgh Instruments FLSP920 spectrofluorometer with a 980 nm CW laser diode of 90 mW as an excitation source. A 940 nm long pass filter was placed between the 980 nm laser and the measured nanoparticles to ensure only the 980 nm radiation as the excitation. The power of the 980 nm CW laser diode was measured with a Scientech 364 power energy meter connected to a Scientech 360401 calorimeter. The 940 nm long pass filter was placed between the 980 nm laser and the calorimeter to simulate the actual environment of PL measurement. The area of the laser beam was measured with an IR detector card (Roithner Lasertechnik HT111) located at the sample stage of the PL spectrofluorometer. The power density was then determined to be ~0.5 W/cm^2. No saturation effect was observed in the range of 35 to 140 mW. Raman spectra were taken using 488 nm laser line of an air cooled Ar-ion laser and were recorded at room temperature using a Horiba Jobin Yvon HR800 spectrometer with a charge-coupled device (CCD) detector. Raman spectra of both GdF_3 and YF_3 were taken under identical conditions. Magnetization as a function of applied magnetic field was measured using a Lakeshore 7407 vibrating sample magnetometer at 293 K ranging from −20 to 20 kOe.